Extrapolating Satellite Winds to Turbine Operating Heights

Merete Badger, Alfredo Peña, and Andrea N. Hahmann

Department of Wind Energy, Technical University of Denmark, Roskilde, Denmark

Alexis A. Mouche

IFREMER/LOS, Plouzané, France

Charlotte B. Hasager

Department of Wind Energy, Technical University of Denmark, Roskilde, Denmark

(Manuscript received 10 July 2015, in final form 4 December 2015)

ABSTRACT

Ocean wind retrievals from satellite sensors are typically performed for the standard level of 10 m. This restricts their full exploitation for wind energy planning, which requires wind information at much higher levels where wind turbines operate. A new method is presented for the vertical extrapolation of satellite-based wind maps. Winds near the sea surface are obtained from satellite data and used together with an adaptation of the Monin–Obukhov similarity theory to estimate the wind speed at higher levels. The thermal stratification of the atmosphere is taken into account through a long-term stability correction that is based on numerical weather prediction (NWP) model outputs. The effect of the long-term stability correction on the wind profile is significant. The method is applied to *Envisat* Advanced Synthetic Aperture Radar scenes acquired over the south Baltic Sea. This leads to maps of the long-term stability correction and wind speed at a height of 100 m with a spatial resolution of 0.02°. Calculations of the corresponding wind power density and Weibull parameters are shown. Comparisons with mast observations reveal that NWP model outputs can correct successfully for long-term stability effects and also, to some extent, for the limited number of satellite samples. The satellite-based and NWP-simulated wind profiles are almost equally accurate with respect to those from the mast. However, the satellite-based maps have a higher spatial resolution, which is particularly important in nearshore areas where most offshore wind farms are built.

1. Introduction

Ocean wind retrieval from active microwave sensors on board satellites has been feasible since the early 1990s, when empirical relationships were established between observations of radar backscatter from the sea surface and winds at the height of 10 m (Stoffelen and Anderson 1993). Since then, the archives of both satellite observations and offshore in situ data have grown, and the geophysical model functions (GMFs) used for wind retrieval have been validated and improved (Stoffelen and Anderson 1997b; Quilfen et al. 1998; Hersbach et al. 2007; Hersbach 2010). Wind retrieval is now performed operationally from global-coverage scatterometer data or on demand from higher-resolution synthetic aperture radar (SAR) systems. The ocean wind fields are used for many applications including data assimilation in weather forecast models (Stoffelen and Anderson 1997a; Yu et al. 2015; Fan et al. 2013), ocean modeling (Sivareddy et al. 2015), and climate studies (Fore et al. 2014). This paper focuses on the use of satellite wind fields for wind resource mapping offshore.

The installed wind power capacity offshore is currently increasing by 50% per year and a steady growth is foreseen for the coming years, especially in Europe (Navigant Research 2014). The size of wind turbine generators has also increased dramatically. State-of-the-art turbines designed for offshore conditions have a capacity of 5–8 MW, and they are typically installed at hub heights of 100–140 m. Wind observations are required to

Corresponding author address: Merete Badger, Department of Wind Energy, Technical University of Denmark, Frederiksborgvej 399, 4000 Roskilde, Denmark.
E-mail: mebc@dtu.dk

DOI: 10.1175/JAMC-D-15-0197.1

optimize the positioning of offshore wind farms. Direct measurements at sea are extremely costly and therefore only available for few sites and restricted time periods. Satellite data can give the horizontal wind variability with temporal coverage of more than 20 yr. New and upcoming satellite missions ensure a continuous delivery of data for the future. Examples include the International Space Station (ISS)-RapidScat (NASA 2015), the SAR missions *Sentinel-1 A* and *Sentinel-1 B* (ESA 2015a), and the RADARSAT constellation (Canadian Space Agency 2015). These are promising perspectives for further exploitation of satellite winds in connection with offshore wind resource assessment where the highest possible number of samples is desired (Monaldo et al. 2014).

The application of satellite winds to plan offshore wind farms has been limited so far because of two inherent features of the satellite data. The first is the restricted sampling that polar-orbiting satellites can provide. Snapshots are acquired at fixed times of the day and the diurnal wind variability is not properly accounted for. A combination of wind information from different sensors may facilitate improvements of the diurnal sampling in the near future (Hasager et al. 2015). The second limitation is the lack of data above the 10-m vertical level. The wind energy industry is primarily interested in the wind conditions at the heights where turbines operate. Vertical extrapolation is thus needed to bring the 10-m satellite winds to higher levels. Although the ultimate goal is to map the wind power production, accurate and detailed mapping of the mean wind speed is in itself an important achievement because of the lack of other wind observations offshore.

Numerical weather prediction (NWP) models can be run for years or decades, and they provide time series outputs at many vertical levels. However, the simulations do not always reproduce the real temporal and spatial wind variability with sufficient accuracy and detail for wind energy applications. Reasons for this include inaccuracies in the models and their parameterizations and the coarse temporal and spatial resolution of the input data needed to drive the models (e.g., the atmospheric initial and boundary conditions, sea surface temperature, land cover, topography), which limits the accuracy and the resolution that can be achieved for the model output (Vincent and Hahmann 2015). Further, most operational NWP models do not include the two-way momentum coupling between the ocean surface and the atmosphere above, except in experimental models used for hurricane forecasting (Chen et al. 2013). The uncertainty on wind resource mapping based on NWP modeling varies from region to region. Studies over the North and Baltic Seas have shown a mean absolute error of 5% on the annual mean wind speed, but larger errors are found at more complex offshore sites (Hahmann et al. 2015). Here the satellite winds can provide further insight.

The objective of this paper is to present a new method for vertical extrapolation of satellite winds from 10 m to higher levels within the atmospheric boundary layer. Our approach is to include a long-term correction for atmospheric stability effects, obtained from NWP model outputs and an adaptation of Monin–Obukhov similarity theory (MOST), for the vertical wind extrapolation. Long-term here refers to the overall stability conditions over a period of at least one full year.

The long-term stability correction can be used together with the average 10-m wind speed for each grid cell in the satellite wind maps to extrapolate the wind speed without any use of in situ observations. We hypothesize that a combination of satellite observations at the sea surface and NWP modeling in three dimensions can improve the absolute accuracy and the spatial resolution of wind resource predictions for wind turbine operating heights compared to either of the two data types alone.

The paper is divided into six sections. Section 2 provides background information about satellite-derived winds and vertical wind extrapolation. Section 3 describes the datasets used in our analysis, and section 4 outlines the methodology and results followed by a discussion in section 5 and conclusions in section 6.

2. Background

Capps and Zender (2009, 2010) estimated the global ocean wind power potential at different vertical levels based on 10-m QuikSCAT winds. MOST was applied for atmospheric stability correction of the vertical wind profile using input from a global ocean-surface heat flux product and reanalysis data. The average global wind power estimate increased by 60% from 10 to 100 m with a smaller vertical increase for the tropics and a larger one for the extratropics (Capps and Zender 2010). The accuracy and the regional variability of these estimates are yet unknown since no direct validation was carried out. Scatterometer observations near the coastline are masked by the data-providing agencies to eliminate mixed land–sea wind vector cells. Coastal seas, however, remain the most important for cost-efficient wind power utilization offshore. SAR data cover these areas and will therefore be used for the analyses in this paper.

SAR wind retrieval and quality control is performed by the end users. A comprehensive overview of wind

retrievals from SAR is given by Dagestad et al. (2012). Although it is possible to retrieve winds from SAR over nearshore areas, the accuracy is correlated with the offshore fetch because the GMFs for satellite wind retrievals are tuned to open-ocean wind conditions. Some GMFs are tuned to real wind observations (Stoffelen and Anderson 1997b; Hersbach et al. 2007); others give the equivalent neutral wind (ENW) speed at a height of 10 m (Quilfen et al. 1998; Hersbach 2010). The latter form is the most suitable for vertical wind extrapolation because it is directly related to the wind stress over the sea surface (Portabella and Stoffelen 2009; Liu and Tang 1996).

Information about the atmospheric stability is essential for accurate extrapolation of the wind speed. In the context of satellite wind extrapolation, the stability information is needed for every grid cell over large spatial domains. Since the in situ data availability is too limited, NWP model outputs represent an attractive alternative. Stability information can be obtained from the parameterized heat and momentum fluxes given by a NWP model, but the uncertainty of these fluxes is typically higher than the uncertainties of the modeled wind speeds (Peña and Hahmann 2012; Hahmann et al. 2015). Vertical extrapolation of instantaneous satellite wind samples has previously shown a high uncertainty at the 100-m level compared to mast observations (Badger et al. 2012). Peña and Hahmann (2012) demonstrated how a long-term stability correction can be calculated from standard output parameters of the Weather Research and Forecasting (WRF) Model. This long-term stability correction agreed very well with that estimated from mast observations. Here we assume that a higher accuracy of hub-height winds can be achieved from applying a long-term stability correction to the yearlong average wind speed, as opposed to correcting individual wind samples from satellites with a collocated stability parameter from NWP outputs.

Kelly and Gryning (2010) developed an analytical formulation of the probability density function P of atmospheric stability in terms of $1/L$, where L is the Obukhov length. This formulation overcomes a problem related to averaging of atmospheric stability conditions: A simple calculation of a mean L via mean values of the heat flux and friction velocity, and using this with standard Monin–Obukhov similarity functions, will not lead to correct wind speed estimates because of the nonlinear influence of atmospheric stability upon the mean wind profile. The analytical formulation has been successfully evaluated against observed distributions of $1/L$ over periods longer than one year at five different land sites (Kelly and Gryning 2010) and an offshore site (Peña and Hahmann 2012), and against simulated $1/L$-distributions at more than 10 sites in the North and Baltic Seas (Peña et al. 2012).

Kelly and Gryning (2010) also developed a probabilistic adaptation of the MOST-based wind profile, which makes use of the analytical formulation, that is, the long-term stability correction. They evaluated such an adaptation against average wind speed observations at two sites in northern Europe with measurements up to ~200 m and found very good agreement. The long-term correction is somewhat artificial as it does not express the average stability conditions directly. The long-term stability correction can switch from positive to negative values with varying height because it combines both stable and unstable terms. For stability correction of instantaneous wind speeds, in contrast, the stable and unstable corrections to the wind profile are applied separately.

A clear advantage of the long-term stability correction over instantaneous stability corrections is that we avoid computing wind speeds for conditions in which MOST (and thus the MOST-like stability corrections) should not be applied because the values of the instantaneous stability or the heights of interest are outside the ranges of MOST validity. MOST is valid for describing turbulent fluxes within the surface layer (Lange et al. 2004; Högström et al. 2006). At higher levels, it has limitations when analyzing data on an instantaneous basis (i.e., 10–30-min sampling), especially for stable conditions. The probabilistic adaption of MOST can be applied up to the turbine operating height because the long-term stability correction is within the ranges where MOST is valid. In neutral and unstable conditions, MOST can be applied within the first 200 m (Peña et al. 2008).

One disadvantage of using the long-term stability correction for wind extrapolation is that individual samples of the wind speed are not preserved. Because the power generated by a wind turbine is a highly nonlinear function (roughly a truncated cubic) of wind speed, Jensen's inequality (Jensen 1906) dictates that the mean power cannot be computed from the mean wind speed but must rather be computed by averaging the instantaneous power. Here we present a method for approximation of the wind power aloft from the instantaneous wind samples at 10 m. Further research is needed to fully alleviate the problem.

3. Data and preprocessing

Our analysis is carried out over the southern part of the Baltic Sea, which is bounded by Denmark, Sweden, Germany, and Poland. The area is defined by the longitude range 12°–16°E and the latitude range 54°–56°N. Data from satellite SAR, NWP modeling, and an

offshore research platform are collected and preprocessed for the area.

a. Satellite SAR winds

Envisat Advanced SAR (ASAR) scenes from the European Space Agency (ESA 2015b) are processed to maps of the instantaneous wind speed at the 10-m level. *Envisat* ASAR was an active microwave sensor, which operated at C band during the years 2002–12. The wide swath mode (WSM) with either vertical (VV) or horizontal (HH) polarization in transmit and receive and a spatial resolution of 150 m is used here. Before the wind retrieval, the SAR data are resampled to a gridcell size of 1 km using simple boxcar averaging to reduce inherent noise in the images.

We retrieve wind speeds from the satellite scenes using the C-band GMF called CMOD-IFR2 (Quilfen et al. 1998). This GMF is chosen because it is tuned to buoy observations of the ENW. For the scenes acquired with HH polarization, the polarization ratio of Mouche et al. (2005) with azimuth-angle dependence is applied to account for the lower radar backscatter compared to data with VV polarization. This is necessary because the GMFs for wind retrieval at C band are developed for VV polarization. The wind direction input, which is needed to retrieve the wind speed from SAR, comes from the European Centre for Medium-Range Weather Forecasts model (ECMWF 2015). The model outputs are resampled to match the 1-km satellite data grids.

The SAR-to-wind processing chain was originally established to map a larger domain for the Northern Seas Wind Index Database (NORSEWInD; http://www.norsewind.eu/norse/index.php/database). The dataset was previously compared to wind speed observations from offshore masts in the North Sea and showed correlation coefficients (R^2) of 0.8–0.9 and root-mean-square errors (RMSEs) in the range 1.3–1.5 m s^{-1} at two stations where high-quality wind and temperature observations are available such that the ENW can be obtained (Hasager et al. 2015). In the North Sea, there was a consistent negative mean error (ME) of −0.3 m s^{-1} on the SAR ENW at 10 m. Retrievals of the SAR ENW with an alternative GMF, CMOD5.n, gave a larger but positive ME of 0.6–0.7 m s^{-1}.

To combine all the wind maps from SAR in a statistical analysis for establishing the wind climate at 10 m and higher levels, the area of interest is divided into regular grid cells with a size of 0.02° in the longitudinal and latitudinal directions. All maps presented in this paper are displayed on this grid. The number of overlapping SAR scenes varies from one grid cell to the next, ranging from 583 to 941 samples (Fig. 1).

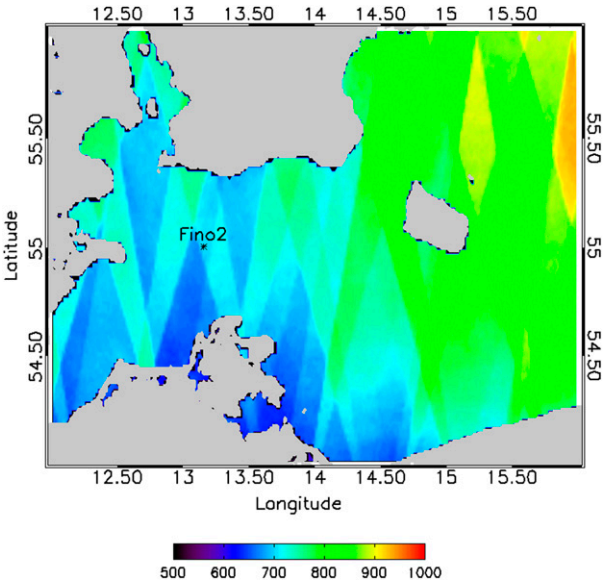

FIG. 1. Number of overlapping *Envisat* ASAR scenes for the domain in the south Baltic Sea. The location of the research platform Fino-2 is indicated (asterisk).

b. NWP modeling

We use output from simulations of the WRF Model (Skamarock et al. 2008). The model setup and the way the simulations are run and combined, which is optimized for estimating wind energy resources, is described in Hahmann et al. (2015). Our WRF Model data cover the years 2006–11. Hourly outputs from a nested domain with the horizontal spacing 5 km × 5 km are used here. The WRF Model outputs needed for this analysis are the friction velocity (UST), the air temperature at 2 m (T2), and the surface heat flux (HFX). In addition, the simulated WRF Model wind speeds (WSPD) at 10, 80, and 100 m are used for comparison with our extrapolated wind speeds. All the WRF Model parameters are regridded to match the 10-m average wind speed maps from SAR (0.02° latitude and longitude).

The hourly WRF Model data are sampled temporally in three different ways before they are combined with any SAR data. The first sampling strategy is to use WRF Model samples that are collocated in time with the SAR observations. The WRF Model sample closest to the SAR data acquisition time is chosen such that the maximum time difference per collocated data pair is 30 min. The second strategy is to use all WRF Model data from the 2-yr period 2010–11, which is fully covered by the meteorological mast observations at Fino-2 (see section 3c). The third sampling strategy is to use all available WRF Model simulations, which cover the 6-yr period 2006–11.

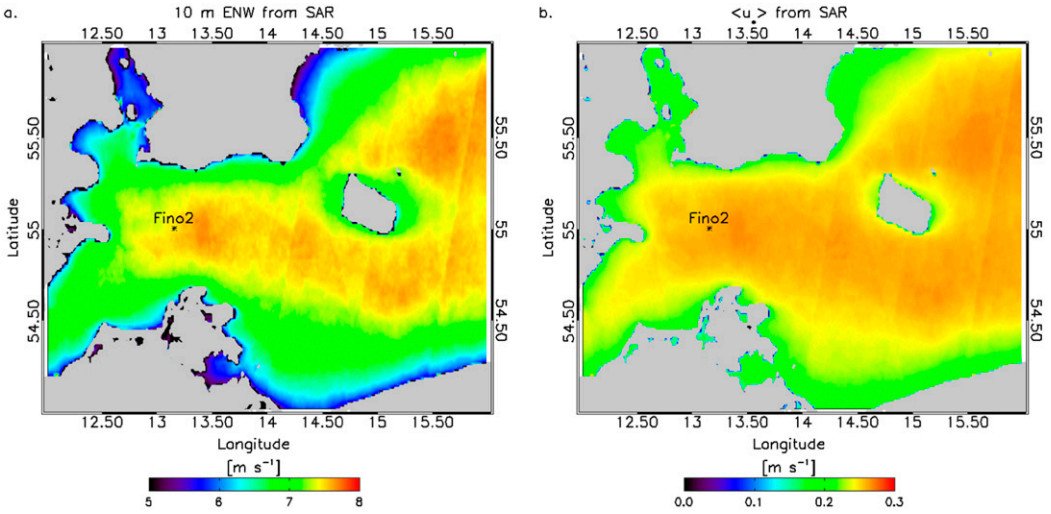

FIG. 2. Maps of (a) the 10-m average wind speed (ENW) from SAR and (b) the average friction velocity $\langle u_* \rangle$. Fino-2 is indicated (asterisk), and the ENW is 7.5 m s^{-1} for that position.

c. *Mast observations*

At the German research platform Fino-2 in the south Baltic Sea, winds and other meteorological parameters are measured. The platform is located at 55°00′24.94″N and 13°09′15.08″E and has delivered data since 31 July 2007. The supply of wind observations was, however, inconsistent for the first few years of operation. The wind speed is measured at eight levels between 32 and 102 m. For this analysis, two full years (2010–11) of wind speed and direction data are used because the data availability is 89% or above at all the measurement heights. The data are recorded as 10-min values. The air temperature is also measured at different levels at Fino-2. Since many assumptions must be made to estimate the atmospheric stability from the observed air temperatures, stability corrections would be highly uncertain. Therefore, we only use the wind speed measurements for evaluation in this analysis.

4. Method and results

In the following, we describe the four main steps in the procedure of estimating wind resources at wind turbine operating heights based on SAR and the WRF Model combined. These include calculations of the friction velocity (section 4a), the atmospheric stability correction (section 4b), wind profiles (section 4c), and wind resources (section 4d).

a. *Friction velocity*

The sea surface friction velocity u_* can be obtained from the diabatic wind profile:

$$u(z) = \frac{u_*}{\kappa}\left[\ln\left(\frac{z}{z_0}\right) - \psi_m\right], \tag{1}$$

where u is the wind speed at the height z and κ is the von Kármán constant (~0.4). The parameter ψ_m is a correction for atmospheric stability effects that is described further below. The sea surface roughness length z_0 can be estimated from Charnock (1955):

$$z_0 = \alpha_c \frac{u_*^2}{g}, \tag{2}$$

where α_c is Charnock's parameter, here set to 0.0144 as in Peña and Hahmann (2012), and g is the gravitational acceleration of Earth. Equations (1) and (2) can be combined and solved iteratively to estimate u_* if the wind speed at a single level is known.

Here, Eq. (1) is applied with $\psi_m = 0$ to estimate u_* because we use the 10-m instantaneous ENW retrieved from individual SAR scenes as our starting point. The ENW is by definition proportional to the wind stress over the sea surface under neutral conditions (Portabella and Stoffelen 2009).

1) FRICTION VELOCITY FROM SAR

Figure 2a shows the average ENW from SAR at 10 m. The wind speed values range from about 5 m s^{-1} near the coastlines to 8 m s^{-1} in the central parts of the south Baltic Sea. Diagonal stripes are artifacts caused by the SAR image edges or by the variable number of overlapping samples (see Fig. 1). The map shows clear gradients of the wind speed along the coastlines, whereas the variability is attenuated over the central parts of the basin. Figure 2b shows a map of the average friction velocity $\langle u_* \rangle$. It ranges from 0.13 m s^{-1} near the coastlines to 0.83 m s^{-1} in the central parts of the domain. The map provides the basis for all vertical

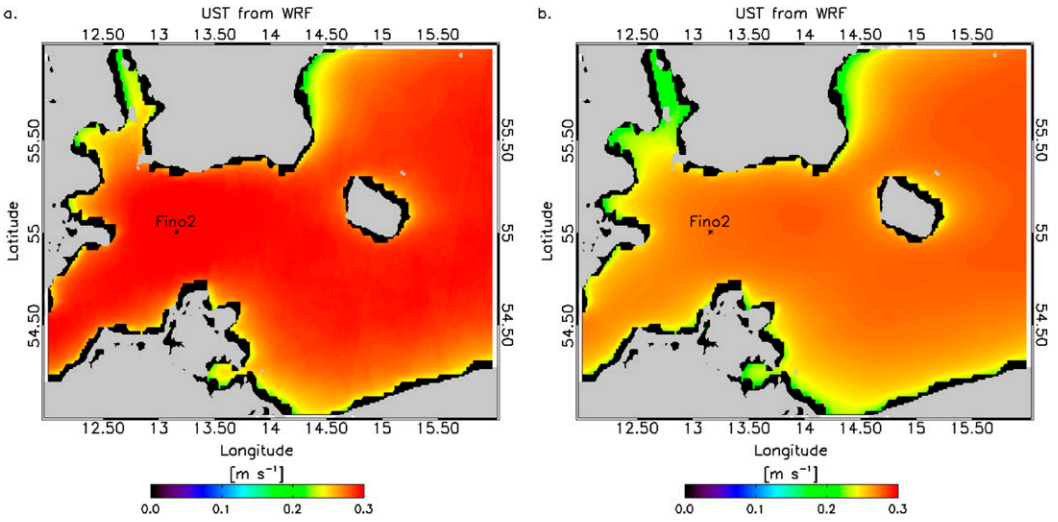

FIG. 3. Average values of the WRF Model parameter UST for (a) WRF Model data collocated with SAR observations and (b) all WRF Model data from 2010–11. WRF Model grid cells contaminated by land effects are masked out (black). The position of Fino-2 is indicated (asterisk).

wind extrapolation of SAR data in the subsequent analysis.

2) FRICTION VELOCITY FROM THE WRF MODEL

The average friction velocity mapped from WRF Model data collocated with SAR in Fig. 3a shows higher values than the map obtained from SAR itself. At Fino-2, friction velocities of 0.26 and 0.30 m s^{-1} are found from SAR and the WRF Model, respectively. The longer WRF Model time series covering 2010–11 (Fig. 3b) and 2006–11 (not shown) are very similar and have the same value of 0.28 m s^{-1} at Fino-2. The spatial variability is similar for all of the WRF Model–based maps and smoother than that for the SAR-based map. Because of the coarser spatial resolution of the WRF Model data, the high friction velocities over land impact the offshore grid cells that are in close proximity to the land. These areas are masked out.

b. *Atmospheric stability correction*

Atmospheric stability can be expressed through the Obukhov length L:

$$L = -\frac{\overline{T}u_*^3}{\kappa g \overline{\omega'\theta_v'}}, \tag{3}$$

where $\overline{T}$ is the mean air temperature, $\overline{\omega'\theta_v'}$ is the kinematic virtual heat flux, ω is the vertical wind velocity component, and θ_v is the virtual potential temperature. The overbars indicate a temporal mean, and the primes indicate fluctuations around the mean value. Three-dimensional observations from high-frequency sonic anemometers are required to measure fluxes of heat and momentum. Since we wish to develop a method for vertical wind extrapolation, which is independent of site observations, the temperature and heat fluxes in Eq. (3) are replaced with parameters from the WRF Model, specifically the air temperature T2 and the heat flux HFX.

Our calculation of instantaneous L values is performed with friction velocity estimates from both SAR and the WRF Model. The former requires collocated sets of SAR and WRF Model data, whereas the latter can be based on WRF Model time series of any length. It is here used for all the three WRF Model sampling strategies. Positive values of the inverse Obukhov length $1/L$ denote stable atmospheric conditions, negative values of $1/L$ denote unstable conditions, and $1/L \sim 0$ represents near-neutral conditions.

To estimate the long-term stability correction, the probability density function P of $1/L$ is calculated from the formulation of Kelly and Gryning (2010),

$$P = n_{\pm}\frac{c_{\pm}}{\sigma_{\pm}}\frac{\exp[-(c_{\pm}|1/L|/\sigma_{\pm})2/3]}{\Gamma[1+(3/2)]}, \tag{4}$$

where the + and − signs denote the sides of the function related to stable and unstable conditions, respectively; $n_{\pm}$ are fractions of occurrence of each stability condition; and $C_{\pm}$ are semiempirical constants (here both are set to 3.0).

The normalized probability density (NPD) function of the inverse Obukhov length ($1/L$) at Fino-2 is plotted in Fig. 4 together with the theoretical distributions, which

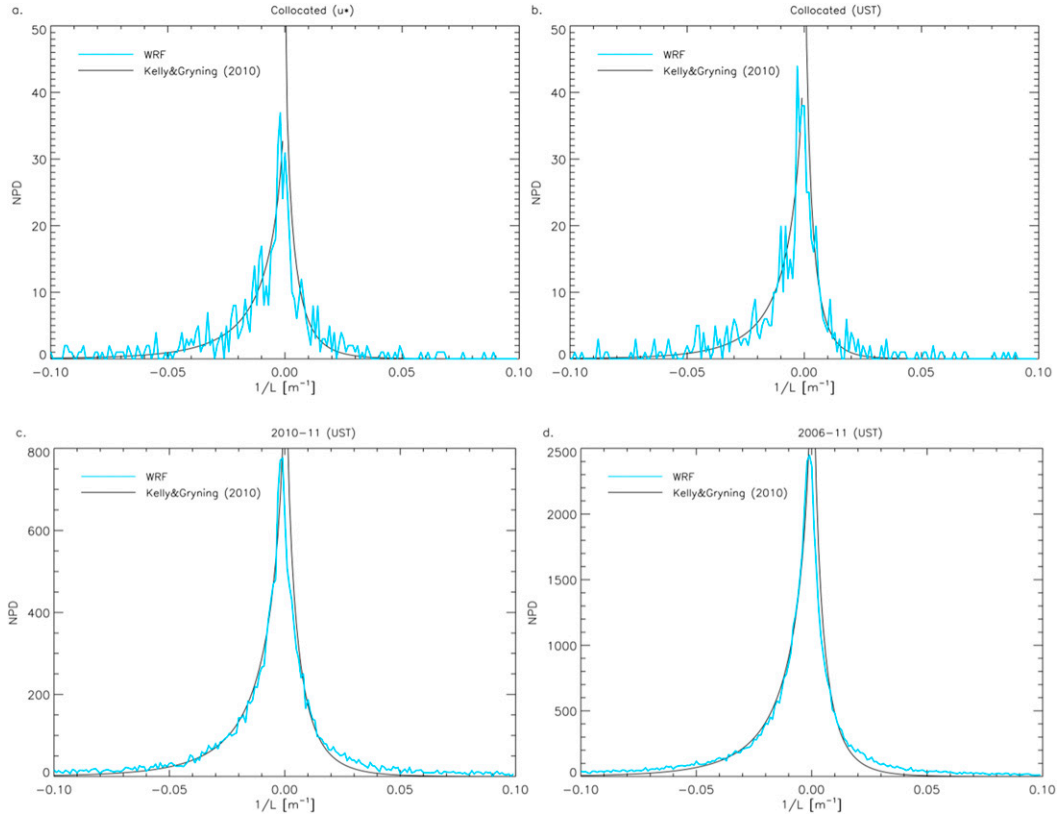

FIG. 4. NPD function of the inverse Obukhov length $1/L$ for the WRF Model grid cell closest to Fino-2 (blue): shown are data for times at which WRF Model outputs are collocated with the SAR using friction velocities derived from (a) SAR (u_*) and (b) WRF (UST), along with all WRF Model outputs (UST) for (c) 2010–11 and (d) 2006–11. Theoretical distributions calculated from Eq. (4) are also shown (black).

can be calculated from Eq. (4). The histograms have a bin size of 0.001 m^{-1} and, as illustrated, the distributions of $1/L$ from our datasets follow the theoretical distributions very well. The 2- and 6-yr WRF Model datasets show smoother curves than the collocated datasets because the number of samples in each histogram bin is larger. For the collocated dataset, each bin contains fewer than 50 samples and some bins have no samples at all. All datasets show a rather symmetric distribution around zero indicating that unstable and stable atmospheric conditions are similarly represented at Fino-2.

The parameters $\sigma_{\pm}$ describe the scales of variations in $1/L$ based on the deviation of the surface heat flux from the average heat flux and the average of the cube of the friction velocity. The calculation of $\sigma_{\pm}$ is performed as

$$\sigma_{\pm} = \frac{g}{\langle \overline{T} \rangle} \frac{\sqrt{\langle (\overline{w'\theta'_v} - \langle \overline{w'\theta'_v} \rangle_{\pm})^2 \rangle}}{\langle u_*^3 \rangle}. \tag{5}$$

Again, we replace the heat flux $\overline{w'\theta'_v}$ with the output HFX from the WRF Model, $\overline{T}$ with T2 from the WRF Model, and u_* with UST from the WRF Model and calculate for all three sampling strategies (angle brackets indicate ensemble averaging). The long-term stability correction ψ_m^* at a given height z can now be calculated for each of the sampling strategies as

$$\psi_m^* = -n_+ \frac{3\sigma_+}{C_+} b' z + n_- f_-, \tag{6}$$

combining the stable (positive) and unstable (negative) contributions. For stable conditions, b' is calculated as

$$b' = \frac{b}{\Gamma(5/2)}, \tag{7}$$

where $b = 4.7$ originates from the standard MOST formulation for stable conditions (Stull 1988):

$$\psi_m\left(\frac{z}{L}\right) = -4.7\frac{z}{L}. \tag{8}$$

Likewise, the calculation of f_- is based on the standard MOST formulation for unstable conditions given by

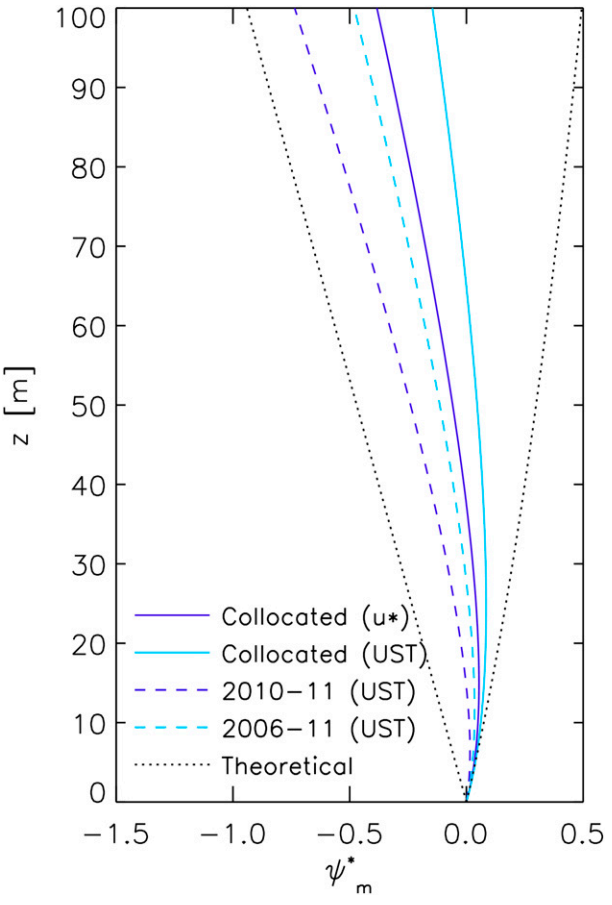

FIG. 5. Vertical distribution of the long-term stability correction ψ_m^* for the WRF Model grid cell closest to Fino-2 using different sampling strategies: collocated with the SAR using friction velocities derived from SAR (u_*) and WRF (UST), all WRF data for 2010–11, and all WRF data for 2006–11. Theoretical boundaries for near-stable (L = 500 m) and near-unstable (L = −500 m) atmospheres are also shown (Gryning et al. 2007).

$$\psi_m\left(\frac{z}{L}\right) = \frac{3}{2}\ln\left(\frac{1+x+x^2}{3}\right) - \sqrt{3}\arctan\left(\frac{2x+1}{\sqrt{3}}\right) + \frac{\pi}{\sqrt{3}}, \quad \text{where} \tag{9}$$

$$x = \left(1 - 12\frac{z}{L}\right)^{1/3}, \quad \text{and so} \tag{10}$$

$$f_- \sim \psi_m\left(\frac{z}{L_{\text{eq}}}\right), \quad \text{where} \tag{11}$$

$$L_{\text{eq}} = \frac{1}{0.4\sigma_-}, \tag{12}$$

thereby taking the scales of variations in $1/L$ into account [see Eq. (5)].

1) PROFILES OF ATMOSPHERIC STABILITY CORRECTION

In Fig. 5, the vertical distribution of the long-term stability correction ψ_m^* at Fino-2 is shown. The profiles show an overall slightly unstable correction from the sea surface and up to 15–30 m. Higher up, a slightly stable correction is found in the long term. Plots for the four datasets divert more and more with increasing height. At 100 m, the long-term stability correction ranges from −0.15 for the collocated dataset generated with UST to −0.74 for the 2-yr WRF Model dataset of 2010–11. All the values are within the theoretical boundaries of the MOST-based near-neutral stability range given by $-500\,\text{m} < L < 500\,\text{m}$ (Gryning et al. 2007).

2) MAPS OF ATMOSPHERIC STABILITY CORRECTION

The spatial variability of ψ_m^* at 100 m is shown in Fig. 6, which reflects the same differences between different sampling strategies as in Fig. 5. The maps based on hourly WRF Model samples have a much smoother appearance than the collocated datasets because the number of samples is high and constant over the entire domain. Differences between the maps in Figs. 6b–d, which are based entirely on WRF Model outputs, can only result from the sampling strategies. In contrast, differences between the maps in Figs. 6a and 6b have to be related to differences in the friction velocity estimates used for the calculation of L and ψ_m^* (i.e., u_* derived from SAR and UST from the WRF Model).

c. *Wind profiles*

The extrapolated wind speed U at any height z is calculated from Eq. (13) with or without the corresponding long-term stability correction ψ_m^*:

$$U(z) = \frac{\langle u_* \rangle}{\kappa}\left[\ln\left(\frac{z}{\langle z_0 \rangle}\right) - \psi_m^*\right]. \tag{13}$$

To distinguish clearly between the wind speeds calculated with and without long-term stability correction, we use the notation ENW for the extrapolated wind speed without stability correction and SDW for the stability-dependent extrapolated winds throughout the rest of this paper. The work flow for calculation of SDW is summarized in Fig. 7.

1) EXTRAPOLATION OF MAST AND WRF MODEL WINDS

Before any SAR data are introduced, self-prediction tests are made on the basis of mast and WRF Model wind speeds to check the validity of the long-term

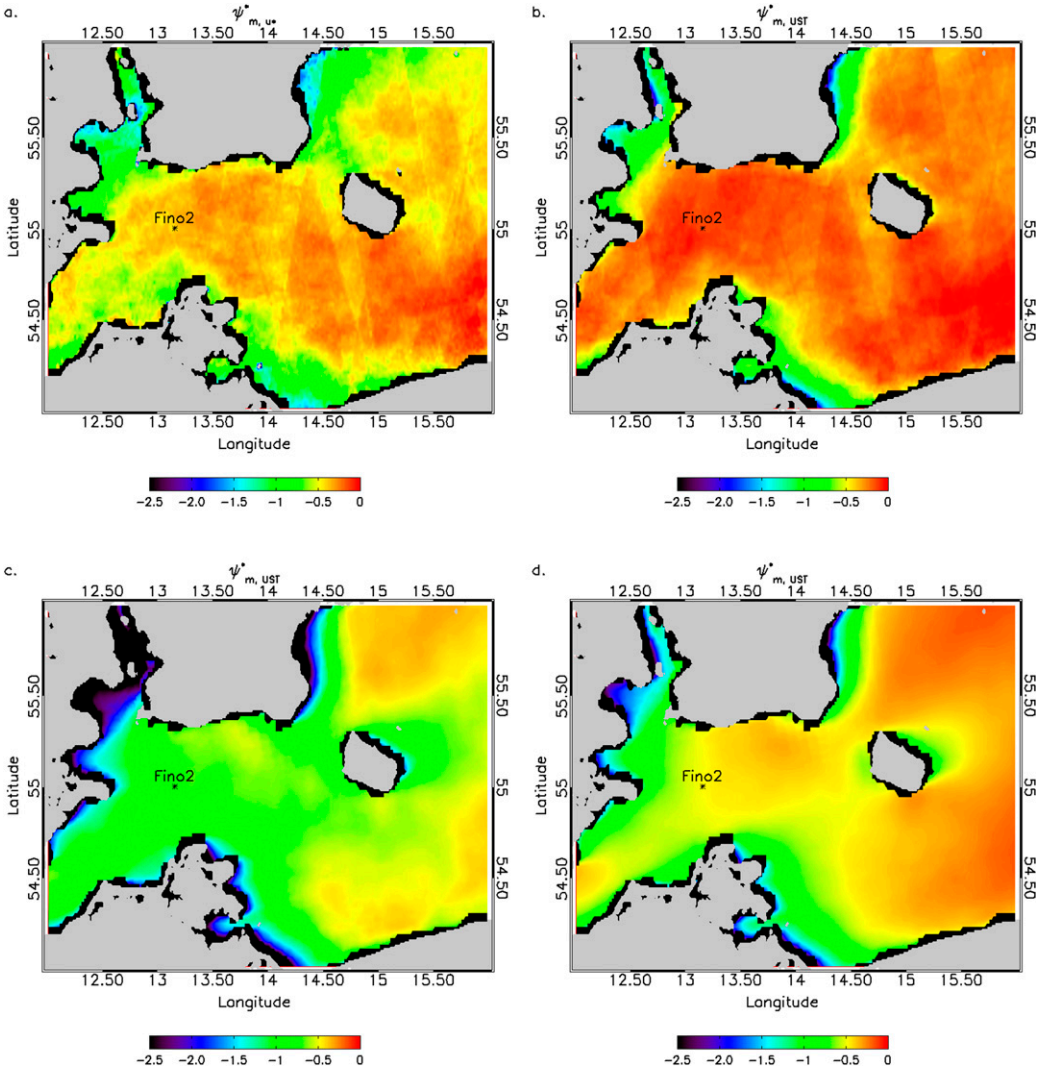

FIG. 6. Long-term stability correction ψ_m^* at 100 m calculated with different sampling strategies for the WRF Model data collocated with the SAR using friction velocities derived from (a) SAR (u_*) and (b) WRF (UST), along with all WRF Model data (UST) for (c) 2010–11 and (d) 2006–11. WRF Model grid cells contaminated by land effects are masked out (black). The position of Fino-2 is indicated (asterisk).

stability correction. Mast observations of wind speed from the lowest measurement height at Fino-2 (32 m) are used in combination with the long-term stability correction from the WRF Model to estimate the $\langle u_* \rangle$ term in Eq. (13) since stability is inherent in the mast observations. The same equation is used again to estimate the winds at higher levels up to 100 m. We perform this estimation with (SDW_{u_*}) and without (ENW_{u_*}) the long-term stability correction.

Similarly, the WRF Model wind speed at the lowest level (10 m) for the grid point closest to Fino-2 is used to estimate the $\langle u_* \rangle$ term in Eq. (13). A second estimate of the friction velocity is made through replacement of the $\langle u_* \rangle$ term with the average friction velocity from the WRF Model output (UST). For both approaches, we estimate the wind speed at higher levels with (SDW_{u_*} and $\mathrm{SDW}_{\mathrm{UST}}$) and without ($\mathrm{ENW}_{u_*}$ and $\mathrm{ENW}_{\mathrm{UST}}$) the long-term stability correction. The extrapolated wind speeds are compared with wind speeds obtained from the mast and from WRF Model output, respectively. This comparison allows uncertainties related to the wind speed extrapolation and the WRF Model–based long-term stability correction to be quantified.

Results of the self-prediction tests are shown in Fig. 8 for the period 2010–11 when mast observations are available. Figure 8a shows wind profiles estimated from vertical extrapolation of the wind observations at the lowest level at the Fino-2 platform (32 m). The

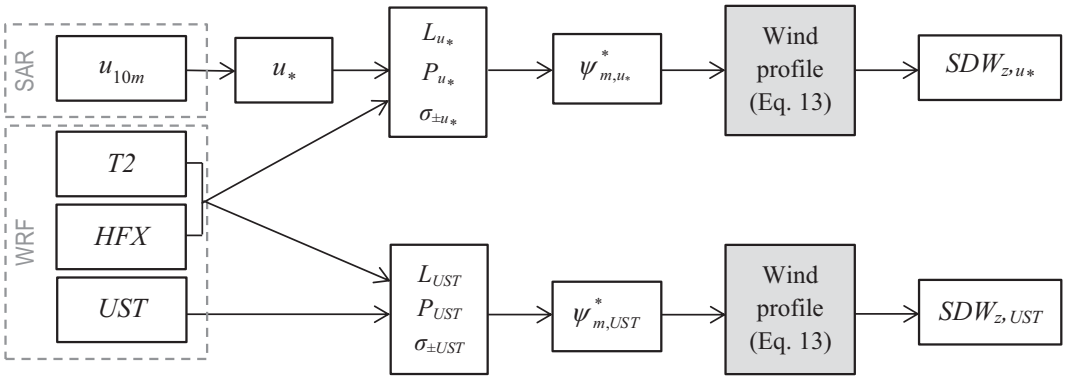

FIG. 7. Illustration of the work flow for calculation of the long-term stability correction and SDW.

consequence of neglecting the long-term stability correction is a wind speed difference of 0.5 m s^{-1} at 100 m. Comparison with the mast observations shows a perfect match at 32 m, which indicates that our extrapolation is consistent such that the wind speed remains the same after extrapolation to the sea surface and back to 32 m. The extrapolated wind speeds fit almost exactly with the mast observations of wind speed at higher levels, except for the top-mounted anemometer at 102 m. The wind speed deviation at the top of the mast is most likely related to a different flow distortion compared with the boom-mounted anemometers at lower measurement levels. Similar effects are reported in other studies (Peña et al. 2012; Westerhellweg et al. 2012) for platforms in the Fino series.

Figure 8b shows wind speeds extrapolated from WRF Model winds at 10 m and also from the WRF Model parameter UST with and without the long-term atmospheric stability correction. The perfect match between the calculated wind speeds and the WRF Model wind at

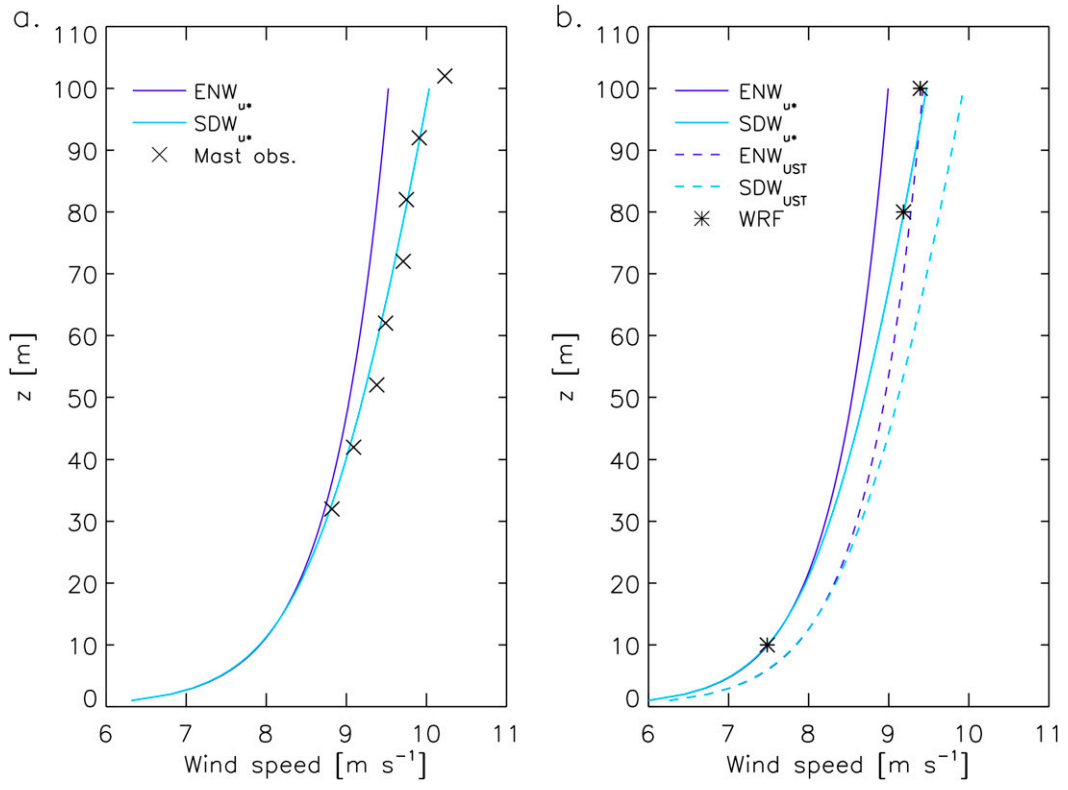

FIG. 8. Self-prediction of wind speeds at Fino-2 for the period 2010–11. The profiles are calculated from (a) the lowest mast observations (32 m) and (b) the lowest WRF Model wind speed level (10 m). Mast observations and WRF Model wind speed data at higher levels are shown for comparison.

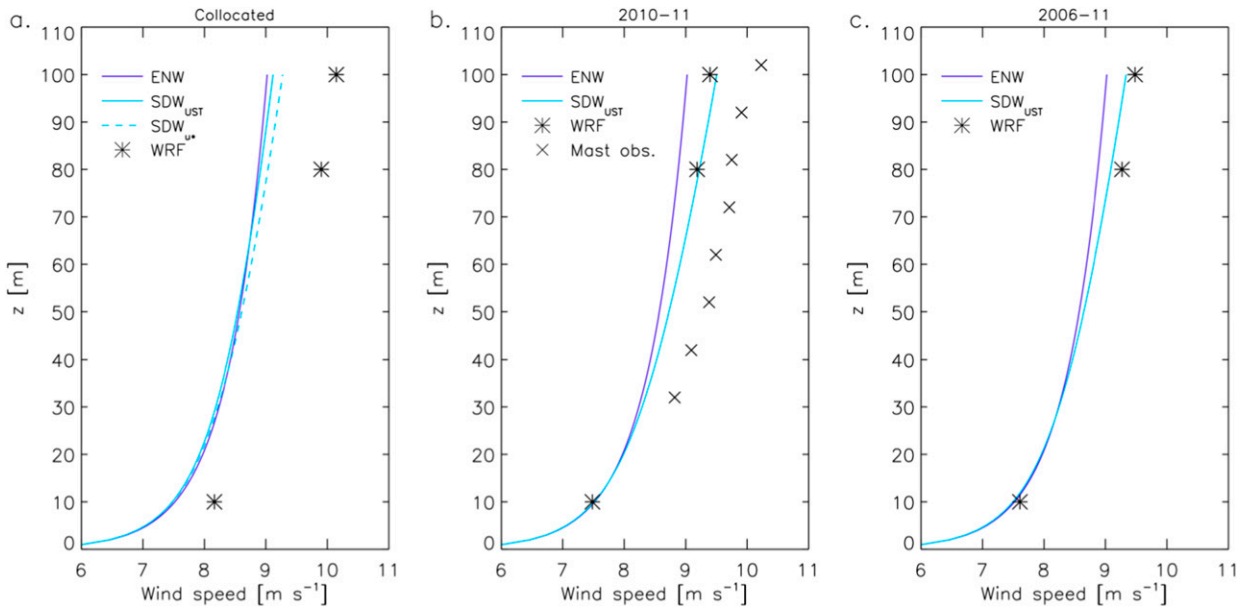

FIG. 9. Wind profiles at Fino-2 calculated from the SAR ENW at 10 m. The long-term stability corrections presented in Fig. 5 are applied. Average wind speeds from the WRF Model and the Fino-2 platform are plotted when available.

10 m confirms the consistency of our method. SDW$_{u_*}$ agrees almost perfectly with the WRF Model wind speeds at 80 and 100 m, whereas SDW$_{UST}$ is higher than the WRF Model wind speeds at the same levels. This finding is consistent with previous studies, which have shown that the WRF Model parameter UST is typically higher than observed values (Peña and Hahmann 2012; Draxl et al. 2014). The consequence of eliminating the long-term stability correction is a wind speed difference of 0.5 m s^{-1} at 100 m.

2) EXTRAPOLATION OF SAR WINDS

Figure 8 confirms that by estimating the long-term stability correction from the WRF Model, we are able to extrapolate wind speeds accurately. We can therefore proceed to the next step where the same method is applied to extrapolate the 10-m SAR winds. The SAR-derived $\langle u_* \rangle$ is combined with the long-term stability correction calculated from the WRF Model. This leads to the main products of our analyses, that is, maps of the extrapolated wind speed at different heights.

Figure 9a shows the wind speed profiles when WRF Model samples collocated with the SAR data acquisitions are used to estimate the ψ_m^* profile. The correction for atmospheric stability is small for the collocated datasets, as also demonstrated in Fig. 5. The two profiles of SDW are therefore close to the profile of ENW. All three profiles show significantly lower wind speeds than the WRF Model wind speed, the lowest being the ENW. At 100 m, the difference is up to 1.1 m s^{-1}.

When 2- and 6-yr time series of WRF Model outputs are used for estimation of the ψ_m^* profile (Figs. 9b,c), differences between the SDW and ENW profiles are reduced to 0.5 m s^{-1} at 100 m. The effect of including the long-term stability correction is thus significant. There is a deviation of 0.2 m s^{-1} between the SDW at 100 m when calculated with the 2 and 6 yr of WRF Model stability information, respectively. This is a result of the larger long-term stability correction toward the stable side for the 2-yr period (see Fig. 5). For both periods, the agreement between the extrapolated SAR winds and WRF Model winds is very good (0.1–0.3 m s^{-1} at 100 m). However, the extrapolated SAR winds and the WRF Model winds all show lower values than those observed at Fino-2 during 2010–11. Further comments to this finding are given in section 5. Table 1 gives a summary of extrapolated and average wind speeds from the different datasets for the 10- and 100-m levels. The extrapolated wind speeds at 100 m are a factor of 1.2–1.3 higher than those at 10 m for all the sampling strategies. The smallest ratio is found for ENW. The reason for missing values is that SDW$_{u_*}$ can only be calculated with collocated SAR and WRF Model data.

3) MAPS OF EXTRAPOLATED SAR WINDS

Maps of the extrapolated wind speed at 100 m calculated from SAR with and without the long-term stability correction from the WRF Model are shown in Fig. 10. Only one WRF Model sampling strategy is presented that covers the period 2010–11. The SDW is consistently

TABLE 1. Extrapolated (SAR) and averaged (WRF Model) wind speeds at Fino-2 ($m\,s^{-1}$). ENW and SDW are the extrapolated SAR winds, and subscripts indicate long-term stability correction based on u_* from SAR or UST from the WRF Model; $\langle u_* \rangle$ is the average friction velocity and N is the number of samples. For comparison, the mast observations at 92 m give an average wind speed of 9.9 $m\,s^{-1}$ during 2010–11. Average friction velocities from the WRF Model are calculated as $\langle \mathrm{UST} \rangle$.

		ENW	SDWu_*	SDW$_{\mathrm{UST}}$	WRF Model
Collocated	100 m	9.0	9.3	9.1	10.1
	10 m	7.5	7.5	7.5	8.2
	$\langle u_* \rangle$	0.26	0.26	0.26	0.30
	N	703	703	703	703
2010–11	100 m	9.0	—	9.5	9.6
	10 m	7.5	—	7.5	7.6
	$\langle u_* \rangle$	0.26	—	0.26	0.28
	N	703	—	703	17 040
2006–11	100 m	9.0	—	9.3	9.6
	10 m	7.5	—	7.5	7.7
	$\langle u_* \rangle$	0.26	—	0.26	0.28
	N	703	—	703	52 560

higher than the ENW in line with the findings at Fino-2. The SAR-based maps are compared to a map of the 100-m average wind speed obtained directly from the WRF Model. As for Fino-2, the absolute wind speeds agree well. The most noticeable differences are the smoother appearance of the WRF Model winds and a difference in the wind speed gradients near the coastlines. The first is due to the lower spatial resolution of WRF Model data or random noise in the original SAR data. The second could result from real wind speed differences or from land contamination of the WRF Model or SAR grid cells closest to the coastline. Land influence would typically reduce the WRF Model wind speed and increase the wind speeds retrieved from SAR.

d. Wind resources

A Weibull fit is made to the SAR and WRF Model wind data populating each grid cell in our domain. The analysis follows the common approach for analysis of meteorological time series in connection with wind energy resource assessment (Troen and Petersen 1989). In contrast to traditional time series analyses, where directional sectors are analyzed separately, the Weibull fitting to SAR wind data is best performed for all directional sectors together because of the limited number of SAR samples (Badger et al. 2010).

Assuming the probability density function of the wind speed follows the Weibull distribution, the wind power density E can be estimated as

$$E = \frac{1}{2}\rho A^3 \Gamma\left(1 + \frac{3}{k}\right), \tag{14}$$

where ρ is the air density (here set to 1.23 $kg\,m^{-3}$) and A and k are the Weibull scale and shape parameters, respectively.

Since the individual wind samples from SAR are not preserved when the wind is extrapolated to higher levels, Weibull fitting cannot be performed after the vertical wind extrapolation. Instead, we perform the Weibull analysis at 10 m and assume a constant relation between the Weibull k parameter from SAR and the WRF Model at all vertical levels. Once the Weibull k parameter is known, the Weibull A parameter is estimated from

$$U = A\Gamma\left(1 + \frac{1}{k}\right). \tag{15}$$

The wind power density for a given height can then be calculated from Eq. (14) using the Weibull k and A estimated for that height.

The shape of the Weibull distribution as expressed by k is assumed to be the same for ENW and SDW at 10 m. We base this assumption on checks made at the two masts Horns Rev M2 and Egmond an Zee in the North Sea, where temperature sensors are available for estimation of atmospheric stability effects. These mast data were used for the analyses of Hasager et al. (2015) and give in both cases a deviation of 0.02 on the k values. At Horns Rev, k for SDW is larger, whereas at Egmond an Zee k for ENW is larger, so no systematic differences on k can be detected on the basis of these datasets. We assume that the same is true in the Baltic Sea.

Results of the Weibull fitting are presented in Table 2. It shows the wind resources calculated at 10 m from SAR and the WRF Model separately and at 100 m from the extrapolated SAR winds, the WRF Model winds, and the mast winds at Fino-2. For the mast, the measurements from the 92-m level are used without any adjustment so the wind resource is expectedly slightly higher at 100 m. The observations at 102 m are neglected because of the deviation from the wind profile at other levels (see Fig. 8a).

At the 10-m level, Weibull k is 2.1 for the SAR dataset, whereas it is 2.5 for all three WRF Model datasets regardless of the sampling. Similar k values are found at 100 m for the WRF Model and also from the mast observations covering the period 2010–11. The Weibull A parameter is directly proportional to the average wind speed. Variations of A and U in Table 2 are thus similar to the variations described above. To summarize, the extrapolated SAR dataset gives consistently lower values of U and A than the WRF Model winds both at 10 and 100 m. Both the SAR-based winds

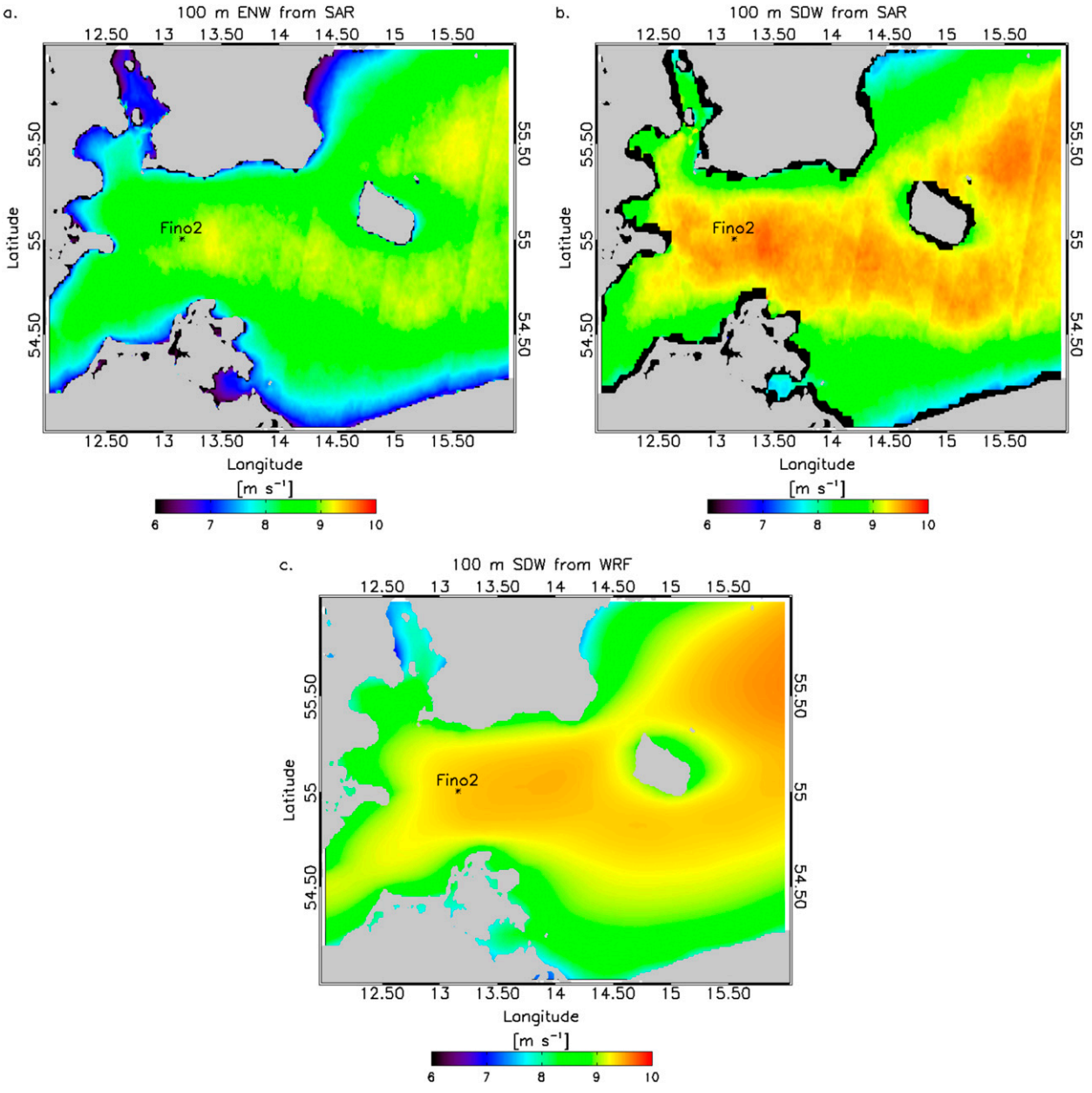

FIG. 10. Wind speed at 100 m calculated from (a) SAR winds without long-term stability correction (ENW), (b) SAR winds with WRF Model long-term stability correction (SDW), and (c) the average WRF Model wind speed. All three maps represent the period 2010–11. In (b), WRF Model grid cells contaminated by land effects are masked out (black).

and the WRF Model winds lead to an underestimation of the U and A calculated from the mast observations.

The best agreement between wind resources from extrapolated SAR and the mast observations is found for the period 2010–11. This is as expected because the two datasets represent the same period. The long-term stability correction from the WRF Model can compensate partly for the infrequent sampling of the SAR data. Results based on WRF Model winds show little deviation between the 2- and 6-yr hourly time series. This finding is supported by previous results of Karagali et al. (2013) showing that the interannual wind variability from the WRF Model in the Baltic Sea is within ±5% of the 10-yr average wind speed. The collocated WRF Model dataset shows higher values of U, A, and E compared to all the other datasets in Table 2. For example, U from the collocated WRF Model is 1.0 m s^{-1} higher than for the SAR-based winds,

TABLE 2. Wind resource parameters at Fino-2 calculated from extrapolated SAR winds (SDW_{UST}), the WRF Model, and mast observations; U is the extrapolated (SAR) and averaged (WRF Model and mast) wind speeds, A and k are the Weibull scale and shape parameters, and E is the wind power density. Mast observations are given for the observation height 92 m.

		10 m		100 m		
	Weibull parameter	SDW_{UST}	WRF Model	SDW_{UST}	WRF Model	Mast observation
Collocated	U (m s^{-1})	7.5	8.1	9.1	10.1	—
	A (m s^{-1})	8.4	9.1	10.2	11.4	—
	k	2.1	2.5	2.1	2.5	—
	E (W m^2)	463	519	808	988	—
2010–11	U (m s^{-1})	—	7.6	9.5	9.6	9.9
	A (m s^{-1})	—	8.6	10.7	10.8	11.2
	k	—	2.5	2.2	2.5	2.5
	E (W m^2)	—	433	930	848	951
2006–11	U (m s^{-1})	—	7.7	9.3	9.6	—
	A (m s^{-1})	—	8.7	10.5	10.9	—
	k	—	2.5	2.2	2.6	—
	E (W m^2)	—	447	892	855	—

whereas the difference is only 0.1–0.3 m s^{-1} for the longer periods.

Despite the slightly lower U and Weibull A values for the extrapolated SAR winds with respect to WRF Model winds, the wind power density is higher for the extrapolated SAR winds than for the WRF Model winds at 100 m. The power density calculated from extrapolated SAR winds is closer to that of the mast observations as a consequence of the different k values described above.

5. Discussion

The results presented here show that the use of an adaptation of MOST in combination with stability information obtained from WRF Model outputs gives accurate estimates of the wind profile for a site in the south Baltic Sea. The WRF Model–based long-term stability correction leads to a 0.5 m s^{-1} reduction of the wind speed at 100 m for this particular site with slightly stable long-term stability correction. This illustrates the importance of thermal effects on the wind climate and the need to account for such effects during vertical wind extrapolation.

Large differences between extrapolated satellite winds and WRF Model winds occur when only the collocated WRF Model data are used to compute the long-term stability correction. This can be explained by two effects: 1) an initial deviation of 0.7 m s^{-1} between the SAR and WRF Model average wind speed at the 10-m level, and 2) effects of atmospheric stability are limited in the morning and in the evening when the satellite scenes were acquired. The collocated WRF Model dataset contains too few samples to represent the long-term stability conditions. Derivation of the long-term stability based on longer time series of WRF Model data (i.e., full years) give a larger correction toward the stable side. This results in very good agreement between the extrapolated satellite winds and the WRF Model wind outputs. Our findings suggest that the long-term stability correction from WRF Model outputs can be used to compensate for the limited number of satellite samples and for the diurnal wind variability that is missing in the satellite data.

Although the sea surface friction velocity derived from the 10-m wind speed leads to more accurate estimates of the wind speed at higher levels than the UST parameter from the WRF Model, it is more feasible to rely on the UST parameter from the WRF Model for estimation of the long-term atmospheric stability. The friction velocity can be derived from SAR winds at the satellite sampling times only, whereas hourly outputs can be obtained from the WRF Model. As stated above, full years of hourly WRF Model data are needed to estimate the long-term stability correction as accurately as possible.

A high level of accuracy on the 10-m satellite wind retrievals is essential for obtaining accurate estimates of the 100-m wind. A large number of validation studies exist in the literature (e.g., Yang et al. 2011; Monaldo et al. 2001, 2004; Hasager et al. 2011), but atmospheric stability effects are rarely accounted for because of a lack of data for the stability correction. The quality of our SAR wind retrievals in the south Baltic Sea is expected to be equivalent to the quality reported for the North Sea in Hasager et al. (2015) because a consistent method has been applied for the wind retrieval. The comparisons in the North Sea also showed a small negative bias on the SAR ENW with respect to stability corrected mast observations. One possible reason for this deviation could be the presence of ocean currents. Winds retrieved from SAR represent the current-relative wind speed (Johannessen et al. 2008), whereas the WRF Model

and mast observations show the atmospheric motions only. The SAR wind retrieval might also be affected by wave breaking and surface slicks (Johannessen et al. 2005; Kudryavtsev et al. 2005).

Our analysis shows that also the WRF Model tends to underpredict the yearlong average wind speed observed at Fino-2. This is consistent with previous work (Hahmann et al. 2015; Peña et al. 2011). The deviation between wind profiles from the WRF Model and the mast might be related to differences of the temporal and spatial scales, which can be resolved by a mesoscale model and an anemometer mounted on a mast. The model integrates wind variability over areas of several square kilometers (in our case 5 km × 5 km grid cells). Anemometer outputs given every 10 min correspond approximately to the spatial scale of the model data. However, the anemometer can be expected to catch more short-term wind variability (i.e., more samples with extremely high or low wind speeds). This might explain the higher wind speed observed at the Fino-2 platform. Flow distortion in the form of speed-up around the anemometers at Fino-2 could be another reason for deviations between the wind speed from SAR, the WRF Model, and the mast.

The Weibull k found from the extrapolated SAR winds at Fino-2 indicates that the wind distribution is different from that calculated from WRF Model winds and mast observations. The reason is likely to be the much lower number of samples in the SAR dataset (703) when compared with the hourly WRF Model winds (17 040) and the 10-min mast observations (93 297). Previous simulation studies indicated that at least 60–70 overlapping SAR scenes are required to estimate the average wind speed and Weibull A within ±10% at the 90% confidence level (Barthelmie and Pryor 2003; Pryor et al. 2004). The studies also show that a much higher number of samples (~2000) are required to achieve the same level of accuracy on Weibull k and the wind power density. The *Envisat* ASAR availability over Fino-2 is 10 times higher than the first requirement, whereas the second requirement cannot be honored. Although our estimates of Weibull k and E from the SAR wind maps can be considered highly uncertain, E calculated from the extrapolated SAR data deviate by only 2.2% from the observations, whereas E from the WRF Model wind data deviate by 10.8% at this site. Consistently with previous studies (Hahmann et al. 2015; Peña et al. 2011), the WRF Model wind distribution is narrower than the observed one.

A growing number of SAR samples from new and upcoming satellite missions (see section 1) are expected to improve the accuracy on SAR-based wind resource estimation at 10 m and therefore also at higher levels. The planned provisioning of level 2 wind fields from *Sentinel-1 A* and *Sentinel-1 B* (ESA 2015a) will shift the wind retrieval processing from the users to the processing facilities and ease the use of SAR wind products for wind energy planning and other applications. The extrapolation method presented here for SAR winds is equally applicable to winds from scatterometers and passive microwave sensors. The sampling frequency is higher for these products, and sampling issues may thus have less influence on the estimated 100-m winds. Extraction of the friction velocities from the satellite data might then be a feasible alternative to the modeled UST parameter.

Fino-2 in the Baltic Sea is a simple test site for the demonstration of our extrapolation method. The site is relatively far from the land with a distance of approximately 40 km to the nearest coastline. Although the atmospheric stability effects have a significant impact on the wind climate for the site, the effects of thermal stratification can be considered limited compared to other areas (Capps and Zender 2009). Analyses at other observation sites around the world would reveal the applicability of our method in different climates.

This analysis is limited to the height interval 0–100 m because this is where the Fino-2 platform provides data for comparison. Offshore wind turbines of the future will be significantly taller and there will thus be a need to extend the wind extrapolation to higher levels. This requires knowledge about the wind profile aloft. Ground-based lidar represents a very promising new way to obtain accurate wind profile observations (Hasager et al. 2008, 2013).

This paper has focused entirely on the benefits of combining satellite winds and NWP modeling for a single purpose: extrapolation of 10-m satellite winds. There are several other ways in which a combination of these two data sources might potentially improve assessment of wind resources offshore: 1) using NWP model outputs of the wind direction during the SAR wind retrieval process, 2) using NWP time series in the order of decades for temporal correction of wind resource estimates, and 3) a full integration of satellite and NWP data can be achieved through assimilation of the 10-m satellite observations into a NWP model (Chang et al. 2015).

6. Conclusions

A new method is presented for vertical extrapolation of satellite winds from 10 m to the heights where offshore wind turbines operate. The fundamental difference from previous efforts in this area is that the wind extrapolation is performed for the yearlong average wind conditions rather than for each instantaneous wind field. This allows a more reliable correction for atmospheric stability effects based on NWP model outputs. The effect of a long-term stability correction is a 0.5 m s^{-1} increase of the

wind speed at 100 m for the analyzed site in the south Baltic Sea. The absolute agreement between extrapolated SAR winds and mast observations is similar to that of WRF Model and mast wind speeds. However, SAR offers a higher level of spatial detail and is based on real observations taking all aspects of air–sea interaction into account. The extrapolation method is also applicable to other types of satellite wind products for which information beyond the 10-m standard output level is desired. Fusion of satellite data and NWP outputs for wind profile prediction has a great potential as it can be applied globally without any need for in situ data, and the applications are wide ranging.

Acknowledgments. This work was supported by the research projects New European Wind Atlas Joint Programme (NEWA, ENER/FP7/618122/NEWA), Northern Seas Wind Index Database (NORSEWInD, TREN-FP7-219048), and South Baltic Offshore Wind Energy Regions (South Baltic OFF.E.R, WTPB.02.02.00-56-004/09). Manuel Goacolou from Collecte Localisation Satellites (CLS) is thanked for reprocessing of SAR wind fields.

REFERENCES

Badger, M., J. Badger, M. Nielsen, C. B. Hasager, and A. Peña, 2010: Wind class sampling of satellite SAR imagery for offshore wind resource mapping. *J. Appl. Meteor. Climatol.*, **49**, 2474–2491, doi:10.1175/2010JAMC2523.1.

——, and Coauthors, 2012: Bringing satellite winds to hub-height. *Proc. EWEA 2012—European Wind Energy Conf. and Exhibition*, Copenhagen, Denmark, EWEA, 9 pp. [Available online at http://orbit.dtu.dk/files/7946190/BRINGING_SATELLITE_WINDS_TO_HUB_HEIGHT.pdf.]

Barthelmie, R. J., and S. C. Pryor, 2003: Can satellite sampling of offshore wind speeds realistically represent wind speed distributions. *J. Appl. Meteor.*, **42**, 83–94, doi:10.1175/1520-0450(2003)042<0083:CSSOOW>2.0.CO;2.

Canadian Space Agency, 2015: RADARSAT Constellation. Accessed 22 October 2015. [Available online at http://www.asc-csa.gc.ca/eng/satellites/radarsat/.]

Capps, S. B., and C. S. Zender, 2009: Global ocean wind power sensitivity to surface layer stability. *Geophys. Res. Lett.*, **36**, L09801, doi:10.1029/2008GL037063.

——, and ——, 2010: Estimated global ocean wind power potential from QuikSCAT observations, accounting for turbine characteristics and siting. *J. Geophys. Res.*, **115**, D09101, doi:10.1029/2009JD012679.

Chang, R., R. Zhu, M. Badger, C. Hasager, X. Xing, and Y. Jiang, 2015: Offshore wind resources assessment from multiple satellite data and WRF modeling over South China Sea. *Remote Sens.*, **7**, 467–487, doi:10.3390/rs70100467.

Charnock, H., 1955: Wind stress on a water surface. *Quart. J. Roy. Meteor. Soc.*, **81**, 639–640, doi:10.1002/qj.49708135027.

Chen, S. S., W. Zhao, M. A. Donelan, and H. L. Tolman, 2013: Directional wind–wave coupling in fully coupled atmosphere–wave–ocean models: Results from CBLAST-Hurricane. *J. Atmos. Sci.*, **70**, 3198–3215, doi:10.1175/JAS-D-12-0157.1.

Dagestad, K.-F., and Coauthors, 2012: Wind retrieval from synthetic aperture radar—An overview. *Proc. SEASAR 2012 Advances in SAR Oceanography*, Tromsø, Norway, ESA, 709. [Available online at http://orbit.dtu.dk/files/59267621/SeaSAR2012_whitepaper_wind.pdf.]

Draxl, C., A. N. Hahmann, A. Peña, and G. Giebel, 2014: Evaluating winds and vertical wind shear from Weather Research and Forecasting Model forecasts using seven planetary boundary layer schemes. *Wind Energy*, **17**, 39–55, doi:10.1002/we.1555.

ECMWF, 2015: Documentation and support: Operational configurations of the ECMWF Integrated Forecasting System (IFS). ECMWF, accessed 22 October 2015. [Available online at http://www.ecmwf.int/en/forecasts/documentation-and-support.]

ESA, 2015a: What is Sentinel-1? ESA, accessed 22 October 2015. [Available online at https://earth.esa.int/web/guest/missions/esa-operational-eo-missions/sentinel-1.]

——, 2015b: What is Envisat? ESA, accessed 22 October 2015. [Available online at https://earth.esa.int/web/guest/missions/esa-operational-eo-missions/envisat.]

Fan, X., J. R. Krieger, J. Zhang, and X. Zhang, 2013: Assimilating QuikSCAT ocean surface winds with the Weather Research and Forecasting Model for surface wind-field simulation over the Chukchi/Beaufort Seas. *Bound.-Layer Meteor.*, **148**, 207–226, doi:10.1007/s10546-013-9805-2.

Fore, A. G., B. W. Stiles, A. H. Chau, B. A. Williams, R. S. Dunbar, and E. Rodríguez, 2014: Point-wise wind retrieval and ambiguity removal improvements for the QuikSCAT climatological data set. *IEEE Trans. Geosci. Remote Sens.*, **52**, 51–59, doi:10.1109/TGRS.2012.2235843.

Gryning, S.-E., E. Batchvarova, B. Brümmer, H. Jørgensen, and S. Larsen, 2007: On the extension of the wind profile over homogeneous terrain beyond the surface boundary layer. *Bound.-Layer Meteor.*, **124**, 251–268, doi:10.1007/s10546-007-9166-9.

Hahmann, A. N., C. L. Vincent, A. Peña, J. Lange, and C. B. Hasager, 2015: Wind climate estimation using WRF model output: Method and model sensitivities over the sea. *Int. J. Climatol.*, **35**, 3422–3439, doi:10.1002/joc.4217.

Hasager, C. B., A. Peña, M. B. Christiansen, P. Astrup, N. M. Nielsen, F. Monaldo, D. Thompson, and P. Nielsen, 2008: Remote sensing observation used in offshore wind energy. *IEEE J. Sel. Top. Appl. Earth Obs. Remote Sens.*, **1**, 67–79, doi:10.1109/JSTARS.2008.2002218.

——, M. Badger, A. Pena, X. G. Larsén, and F. Bingöl, 2011: SAR-based wind resource statistics in the Baltic Sea. *Remote Sens.*, **3**, 117–144, doi:10.3390/rs3010117.

——, D. Stein, M. Courtney, A. Peña, T. Mikkelsen, M. Stickland, and A. Oldroyd, 2013: Hub height ocean winds over the North Sea observed by the NORSEWInD lidar array: Measuring techniques, quality control and data management. *Remote Sens.*, **5**, 4280–4303, doi:10.3390/rs5094280.

——, and Coauthors, 2015: Offshore wind climatology based on synergetic use of Envisat ASAR, ASCAT and QuikSCAT. *Remote Sens. Environ.*, **156**, 247–263, doi:10.1016/j.rse.2014.09.030.

Hersbach, H., 2010: Comparison of C-band scatterometer CMOD5.N equivalent neutral winds with ECMWF. *J. Atmos. Oceanic Technol.*, **27**, 721–736, doi:10.1175/2009JTECHO698.1.

——, A. Stoffelen, and S. de Haan, 2007: An improved C-band scatterometer ocean geophysical model function: CMOD5. *J. Geophys. Res.*, **112**, C03006, doi:10.1029/2006JC003743.

Högström, U., A.-S. Smedman, and H. Bergström, 2006: Calculation of wind speed variation with height over the sea. *Wind Eng.*, **30**, 269–286, doi:10.1260/030952406779295480.

Jensen, J. L. W. V., 1906: Sur les fonctions convexes et les inégalités entre les valeurs moyennes (On convex functions and inequalities between average values). *Acta Math.*, **30**, 175–193, doi:10.1007/BF02418571.

Johannessen, J. A., V. Kudryavtsev, D. Akimov, T. Eldevik, N. Winther, and B. Chapron, 2005: On radar imaging of current features: 2. Mesoscale eddy and current front detection. *J. Geophys. Res.*, **110**, C07017, doi:10.1029/2004JC002802.

——, B. Chapron, F. Collard, V. Kudryavtsev, A. Mouche, D. Akimov, and K.-F. Dagestad, 2008: Direct ocean surface velocity measurements from space: Improved quantitative interpretation of Envisat ASAR observations. *Geophys. Res. Lett.*, **35**, L22608, doi:10.1029/2008GL035709.

Karagali, I., M. Badger, A. N. Hahmann, A. Peña, C. B. Hasager, and A. M. Sempreviva, 2013: Spatial and temporal variability of winds in the northern European seas. *Renewable Energy*, **57**, 200–210, doi:10.1016/j.renene.2013.01.017.

Kelly, M., and S.-E. Gryning, 2010: Long-term mean wind profiles based on similarity theory. *Bound.-Layer Meteor.*, **136**, 377–390, doi:10.1007/s10546-010-9509-9.

Kudryavtsev, V., D. Akimov, J. Johannessen, and B. Chapron, 2005: On radar imaging of current features: 1. Model and comparison with observations. *J. Geophys. Res.*, **110**, C07016, doi:10.1029/2004JC002505.

Lange, B., S. Larsen, J. Højstrup, and R. Barthelmie, 2004: The influence of thermal effects on the wind speed profile of the coastal marine boundary layer. *Bound.-Layer Meteor.*, **112**, 587–617, doi:10.1023/B:BOUN.0000030652.20894.83.

Liu, W. T., and W. Tang, 1996: Equivalent neutral wind. JPL Publ. 96-17, 16 pp. [Available online at http://ntrs.nasa.gov/archive/nasa/casi.ntrs.nasa.gov/19970010322.pdf.]

Monaldo, F. M., D. R. Thompson, R. C. Beal, W. G. Pichel, and P. Clemente-Colón, 2001: Comparison of SAR-derived wind speed with model predictions and ocean buoy measurements. *IEEE Trans. Geosci. Remote Sens.*, **39**, 2587–2600, doi:10.1109/36.974994.

——, ——, W. G. Pichel, and P. Clemente-Colon, 2004: A systematic comparison of QuikSCAT and SAR ocean surface wind speeds. *IEEE Trans. Geosci. Remote Sens.*, **42**, 283–291, doi:10.1109/TGRS.2003.817213.

——, X. Li, W. G. Pichel, and C. R. Jackson, 2014: Ocean wind speed climatology from spaceborne SAR imagery. *Bull. Amer. Meteor. Soc.*, **95**, 565–569, doi:10.1175/BAMS-D-12-00165.1.

Mouche, A. A., D. Hauser, J. F. Daloze, and C. Guerin, 2005: Dual-polarization measurements at C-band over the ocean: Results from airborne radar observations and comparison with ENVISAT ASAR data. *IEEE Trans. Geosci. Remote Sens.*, **43**, 753–769, doi:10.1109/TGRS.2005.843951.

NASA, 2015: Mission to Earth: ISS-RapidScat. JPL, accessed 22 October 2015. [Available online at http://www.jpl.nasa.gov/missions/iss-rapidscat.]

Navigant Research, 2014: Forecast 2014–2018. World market update 2013: International wind energy development. Accessed 30 April 2015.

Peña, A., and A. Hahmann, 2012: Atmospheric stability and turbulence fluxes at Horns Rev—An intercomparison of sonic, bulk and WRF model data. *Wind Energy*, **15**, 717–731, doi:10.1002/we.500.

——, S.-E. Gryning, and C. B. Hasager, 2008: Measurements and modelling of the wind speed profile in the marine atmospheric boundary layer. *Bound.-Layer Meteor.*, **129**, 479–495, doi:10.1007/s10546-008-9323-9.

——, A. N. Hahmann, C. B. Hasager, F. Bingöl, I. Karagali, J. Badger, M. Badger, and N.-E. Clausen, 2011: South Baltic wind atlas: South Baltic Offshore Wind Energy Regions Project. Risø.R-1775(EN), Risø DTU, National Laboratory for Sustainable Energy, 66 pp. [Available online at http://orbit.dtu.dk/fedora/objects/orbit:86024/datastreams/file_5578113/content.]

——, T. Mikkelsen, S.-E. Gryning, C. B. Hasager, A. N. Hahmann, M. Badger, I. Karagali, and M. Courtney, 2012: Offshore vertical wind shear. DTU Wind Energy-E-Rep. 0005, Department of Wind Energy, Technical University of Denmark, 117 pp. [Available online at http://www.orbit.dtu.dk/files/10591005/DTU_Wind_Energy_E_report_0005.pdf.]

Portabella, M., and A. Stoffelen, 2009: On scatterometer ocean stress. *J. Atmos. Oceanic Technol.*, **26**, 368–382, doi:10.1175/2008JTECHO578.1.

Pryor, S. C., M. Nielsen, R. J. Barthelmie, and J. Mann, 2004: Can satellite sampling of offshore wind speeds realistically represent wind speed distributions? Part II: Quantifying uncertainties associated with sampling strategy and distribution fitting methods. *J. Appl. Meteor.*, **43**, 739–750, doi:10.1175/2096.1.

Quilfen, Y., B. Chapron, T. Elfouhaily, K. Katsaros, and J. Tournadre, 1998: Observation of tropical cyclones by high-resolution scatterometry. *J. Geophys. Res.*, **103**, 7767–7786, doi:10.1029/97JC01911.

Sivareddy, S., M. Ravichandran, M. S. Girishkumar, and K. V. S. R. Prasad, 2015: Assessing the impact of various wind forcing on INCOIS-GODAS simulated ocean currents in the equatorial Indian Ocean. *Ocean Dyn.*, **65**, 1235–1247, doi:10.1007/s10236-015-0870-6.

Skamarock, W. C., and Coauthors, 2008: A description of the Advanced Research WRF version 3. NCAR Tech. Note NCAR/TN-475+STR, 113 pp., doi:10.5065/D68S4MVH.

Stoffelen, A., and D. L. T. Anderson, 1993: Wind retrieval and ERS-1 scatterometer radar backscatter measurements. *Adv. Space Res.*, **13**, 53–60, doi:10.1016/0273-1177(93)90527-I.

——, and ——, 1997a: Ambiguity removal and assimilation of scatterometer data. *Quart. J. Roy. Meteor. Soc.*, **123**, 491–518, doi:10.1002/qj.49712353812.

——, and D. Anderson, 1997b: Scatterometer data interpretation: Estimation and validation of the transfer function CMOD4. *J. Geophys. Res.*, **102**, 5767–5780, doi:10.1029/96JC02860.

Stull, R. B., 1988: *An Introduction to Boundary Layer Meteorology*. Kluwer Academic, 666 pp.

Troen, I., and E. L. Petersen, 1989: European wind atlas. Risø National Laboratory, 656 pp. [Available online at http://orbit.dtu.dk/files/112135732/European_Wind_Atlas.pdf.]

Vincent, C. L., and A. N. Hahmann, 2015: The impact of grid and spectral nudging on the variance of the near-surface wind speed. *J. Appl. Meteor. Climatol.*, **54**, 1021–1038, doi:10.1175/JAMC-D-14-0047.1.

Westerhellweg, A., T. Neumann, and V. Riedel, 2012: FINO1 mast correction. *DEWI Mag.*, **40**, 60–66. [Available online at http://www.dewi.de/dewi_res/fileadmin/pdf/publications/Magazin_40/09.pdf.]

Yang, X., X. Li, W. G. Pichel, and Z. Li, 2011: Comparison of ocean surface winds from ENVISAT ASAR, MetOp ASCAT scatterometer, buoy measurements, and NOGAPS model. *IEEE Trans. Geosci. Remote Sens.*, **49**, 4743–4750, doi:10.1109/TGRS.2011.2159802.

Yu, Y., W. Zhang, Z. Wu, X. Yang, X. Cao, and M. Zhu, 2015: Assimilation of HY-2A scatterometer sea surface wind data in a 3DVAR data assimilation system—A case study of Typhoon Bolaven. *Front. Earth Sci.*, **9**, 192–201, doi:10.1007/s11707-014-0461-8.